Hole-Trapping-Induced Stabilization of Ni^{4+} in $SrNiO_3/LaFeO_3$ Superlattices

Le Wang, Zhenzhong Yang, Mark E. Bowden, John W. Freeland, Peter V. Sushko, Steven R. Spurgeon, Bethany Matthews, Widitha S. Samarakoon, Hua Zhou, Zhenxing Feng, Mark H. Engelhard, Yingge Du, and Scott A. Chambers**

Dr. L. Wang, Dr. Z. Yang, Dr. P. V. Sushko, Dr. Y. Du, Dr. S. A. Chambers
Physical and Computational Sciences Directorate, Pacific Northwest National Laboratory, Richland, Washington 99354, USA
E-mail: yingge.du@pnnl.gov; sa.chambers@pnnl.gov
Dr. M. E. Bowden, Dr. M. H. Engelhard
Environmental Molecular Sciences Laboratory, Pacific Northwest National Laboratory, Richland, Washington 99352, USA
Dr. J. W. Freeland, Dr. H. Zhou
Advanced Photon Source, Argonne National Laboratory, Lemont, Illinois 60439, USA
Dr. S. R. Spurgeon, Dr. B. Matthews
Energy and Environment Directorate, Pacific Northwest National Laboratory, Richland, Washington 99352, USA
W. S. Samarakoon, Prof. Z. Feng
School of Chemical, Biological and Environment Engineering, Oregon State University, Oregon 97331, USA

Keywords: charge transfer, octahedral rotation, Ni^{4+}, Fe^{4+}, superlattices

Abstract: Creating new functionality in materials containing transition metals is predicated on our ability to control the associated charge states. For a given transition metal, there is an upper limit on valence that is not exceeded under normal conditions. Here we demonstrate that we can exceed this limit of 3+ for Ni and Fe via synthesis of $(SrNiO_3)_m/(LaFeO_3)_n$ superlattices by tuning *n* and *m*. The Goldschmidt tolerance constraints are lifted and $SrNi^{4+}O_3$ with holes on adjacent O anions is stabilized as a perovskite at the single unit cell level (*m* = 1). Holding *m* = 1, spectroscopy reveals that the *n* = 1 superlattice contains Ni^{3+} and Fe^{4+}, whereas Ni^{4+} and Fe^{3+} are observed in the *n* = 5 superlattice. We reveal that the B-site cation valences can be tuned by controlling the magnitude of the FeO_6 octahedral rotations which, in turn, determine the energy balance between Ni^{3+}/Fe^{4+} and Ni^{4+}/Fe^{3+}, thus controlling emergent electrical properties such as the band alignment and resulting hole confinement. We suggest that this approach opens a new avenue for synthesizing novel, metastable layered structures with new functionalities.

Complex transition metal oxides ABO_3, where *A* is a divalent or trivalent ion and *B* is a transition metal (TM) ion, exhibit fascinating properties which include ferroelectricity, superconductivity, colossal magnetoresistance and multiferroicity. The ability to precisely control layer-by-layer epitaxial film growth enables the synthesis of novel combinations of complex oxides in the form of heterostructures and superlattices (SLs), and these have been a rich source of insight into emergent phenomena not seen in bulk phases.[1,2] Charge distribution at these heterointerfaces is a widely studied phenomenon.[3-9] The electronegativity difference between different complex oxides is a common driver of charge redistribution in such systems.[10] In most cases, the O 2*p* band energies align across the interface. Hence, the charge distribution is mainly determined by the energy difference between the occupied and virtual 3*d* orbitals for the TM ions. In this case, the charge transfer energy (Δ), which separates the metal 3*d* and oxygen 2*p* derived bands, becomes a critical parameter in determining the balance of charge. For titanates, the Ti 3*d* bands are ~3 eV higher in energy than the O 2*p* bands, making titanates effective electron donors.[6-8] However, for rare earth nickelates $RNiO_3$ (*R* = La, Pr, Nd, Sm, etc.), the Ni 3*d* bands lie below O 2*p* bands, leading to a negative Δ and strong hybridization between Ni 3*d* and O 2*p* orbitals.[11] As a result, $RNiO_3$ compounds tend to be electron acceptors. Additionally, charge redistribution at correlated oxide interfaces is usually influenced by oxygen octahedral connectivity.[8,12,13] Grisolia *et al.* observed that, in addition to differences in electronegativity and polar effects at $GdTiO_3/RNiO_3$ heterointerfaces, the energy required to alter the covalency of the metal-oxygen bond is another key parameter determining the charge balance.[8] As the ionic radius of the rare-earth A-site cation increases, nickelates exhibit stronger covalent character between Ni 3*d* and O 2*p* orbitals which in turn increases the energy cost of rehybridization during charge rearrangement, thereby limiting the extent of Ti-to-Ni charge transfer.

Following the prediction of high T_c cuprate-like superconductivity physics in $LaNiO_3/LaAlO_3$ (LNO/LAO) SLs,[14,15] a number of heterostructures and SLs involving nickelates, such as $LaNiO_3/LaMnO_3$ (LNO/LMO) and $LaNiO_3/LaTiO_{3+\delta}$ (LNO/LTO), have been extensively investigated.[7,8,16-22] However, very little is known about carrier distribution, even at the isopolar interface of $LaFeO_3$ and LNO (LFO/LNO). Bulk LNO is a paramagnetic metal with the $t_{2g}^6 e_g^2 \underline{L}$ (where $\underline{L}$ indicates the ligand hole) electronic configuration for Ni^{3+},[23] whereas bulk LFO is a charge-transfer insulator ($\Delta \sim 2.3$ eV) with the $t_{2g}^3 e_g^2$ electronic configuration for Fe^{3+}.[24] Based on the electronegativity difference between Ni and Fe, the electronic ground state at the LFO/LNO interface should include the $t_{2g}^3 e_g^2 \underline{L}$[25] and $t_{2g}^6 e_g^2$ electronic configurations for Fe^{4+} and Ni^{2+}, respectively. Substituting Sr for La at the *A* site in LNO causes the O 2*p* band to shift up in energy and move closer to Fermi level, thereby enhancing Ni 3*d*-O 2*p* hybridization and leading to a smaller Δ.[26] However, doing so would force Ni to an unstable, nominal 4+ oxidation state. Superlattice engineering offers a powerful way of modulating the oxygen octahedral connectivity, which in turn may allow an otherwise unstable phase to be stabilized and functionalized.[27-29] Thus, it is of significant interest to explore whether we can stabilize $SrNiO_3$ in a perovskite phase through superlattice integration, and if so, to what extent can we modulate the Ni valence through interfacial charge transfer between Ni and other transition metal cations. To test these hypothesizes, we have grown $SrNiO_3/LaFeO_3$ (SNO/LFO) SLs. In SNO_m/LFO_n SLs, where *m* and *n* denote the number of unit cells (u.c.) of SNO and LFO, respectively, controlling *m* and *n* is thus expected to modulate the oxygen octahedral connectivity which in turn may allow the electronic properties to be tuned.

In this work, we present experimental and first-principles modeling results for a set of $(SNO_m/LFO_n)_k$ SLs designed specifically to answer these questions. We find that SLs with more than one u.c. of SNO ($m > 1$) are poorly ordered crystallographically, consistent with the

instability of SNO as a bulk perovskite. We thus focus on SLs of the form $(SNO_1/LFO_n)_k$, in which perovskite SNO can be uniquely stabilized. To investigate charge distributions, we combine *in situ* x-ray photoelectron spectroscopy (XPS) and *ex situ* x-ray absorption spectroscopy (XAS) with first-principles density functional theory (DFT) calculations. We vary *n* in order to probe the influence of oxygen octahedral connectivity on charge transfer. We find that Ni^{3+} and Fe^{4+} naturally form in the $n = 1$ SL due to electron transfer from Fe to Ni. In contrast, Ni^{4+} and Fe^{3+} are found in the $n = 5$ SL, in which electron transfer is strongly suppressed.

Pure LFO films and all $(SNO_m/LFO_n)_k$ SLs SLs were grown on (001)-oriented $(LaAlO_3)_{0.3}(Sr_2AlTaO_6)_{0.7}$ (LSAT) substrates using oxygen plasma assisted molecular beam epitaxy (OPA-MBE) (see Experimental details in Supporting Information). No well-ordered epitaxial SL structures were observed when $m > 1$, as SNO layers thicker than one u.c. display significant disorder (see **Figure S1**). This structural instability is ascribed to the relatively large ionic radius ratio $R(Sr^{2+})/R(Ni^{4+})$. Previous study reported that the stable bulk structure of $SrNiO_3$ is hexagonal,[30] and thus it does not lattice match to cubic perovskite substrates. This is the most likely reason that no stable $SrFe_{1-x}Ni_xO_3$ structures with $x > 0.5$ have been reported in the literature.[31] However, we show that all-perovskite-structured superlattices can be stabilized when the SNO layer thickness is limited to 1 u.c ($m = 1$). The structural diagram for a generic $(SNO_1/LFO_n)_k$ SL deposited on a buffer layer of 10 u.c. LFO is shown in **Figure 1a**. Figure 1b shows a high-angle annular dark-field (HAADF) scanning transmission electron microscopy (STEM) image of a typical $n = 5$ SL. The expected epitaxial relationship is clearly present, and the interfaces are free of dislocations. Since the LSAT substrates were not chemically etched prior to film deposition, we did not attempt to control the termination of each material. However, the interface structure appears to be $LaO\text{-}FeO_2\text{-}...\text{-}LaO\text{-}FeO_2\text{-}SrO\text{-}NiO_2\text{-}LaO\text{-}FeO_2\text{-}\ldots$ (see the structural model in Figure 1b). Inspection of larger lateral areas (**Figure S2**) reveals that some *A*-site intermixing is suggested by the broadening and double

peak profile of the Sr $L_{2,3}$ intensity in the electron energy loss spectroscopy (EELS) maps. However, steps at the substrate surface may also contribute to this broadening by disrupting the perfect planarity of the single SNO layer.

X-ray diffraction (XRD) patterns (**Figure S3a**) exhibit clear Bragg peaks characteristic of the average out-of-plane lattice parameter (c) in each SL period and SL thickness fringes, indicating good crystallinity. Figure 1c shows XRD θ–2θ scans near the (002) SL reflection for the $(SNO_1/LFO_5)_{10}$ and $(SNO_1/LFO_8)_8$ SLs. The good agreement between experiment and simulations reveals that the SLs exhibit the targeted structures as seen for the n = 5 SL in Figure 1c. With increasing LFO layer thickness, the SL Bragg angle shifts to lower 2θ value (Figure 1c and Figure S3b), indicating that the average c increases with n (Figure S3c). The c value for the n = 8 SL is close to that of the pure LFO film. Inasmuch as the c value of the SL decreases with increasing SNO mole fraction and approaches to that of bulk SNO reported by H. Seki *et al*,[31] our results indicate that we can stabilize perovskite SNO in these SNO_1/LFO_n SLs. All SLs were found to be coherently strained to the LSAT substrates according to reciprocal space maps (RSMs) (Figure S3d). Thickness fringes and superlattice peaks are also clearly seen in the RSM for the n = 8 SL in Figure 1d.

We now consider the effect of n in SNO_1/LFO_n SLs on the valences of Ni and Fe. In order to determine the TM cation valences from XPS data, we shift all Fe 2*p* and Ni 2*p* spectra so that the corresponding O 1*s* peaks fall at 530.0 eV. The results are shown in **Figure 2a** and **Figure S4**. Although there is some contribution from Ni LMM Auger peaks, the overall Fe 2*p* spectrum for the n = 1 SL is very similar to that of Fe 2*p* in fully oxidized $SrFeO_3$ and $BaFeO_3$ thin films, which was straightforwardly interpreted as being due to the presence of Fe^{4+}.[32-34] The Fe $2p_{3/2}$ and $2p_{1/2}$ features become narrower and shift to lower binding energy with increasing n, signaling a decrease in Fe valence. For the n = 5 and 8 SLs,

the Fe 2*p* spectra display a clear satellite feature and the line shape matches well with that of pure $LaFeO_3$, indicating that the Fe valence is 3+. This change is corroborated by XAS measurements collected in total electron yield (TEY) mode at the Fe *L*-edge. TEY mode is sensitive to the near-surface layers (attenuation length of a few nm), which allows us to filter out the contribution from the LFO buffer layer. In Figure 2b we compare the Fe *L*-edge spectra of $n = 1$ and 5 SLs with those for reference films of fully oxidized LFO (Fe^{3+}) and $SrFeO_3$ (Fe^{4+}). For the $n = 5$ SL, the Fe L_3 feature exhibits a well-separated double peak structure, and both the line shape and the peak width match well with those of LFO (Fe^{3+}). In contrast, in the $n = 1$ SL, the double peak structure becomes less obvious and the peak width is similar to that of $SrFeO_3$ which suggests that Fe is mostly Fe^{4+}. In support of this assignment, we note that Mössbauer effect spectra have been measured for $SrFeO_3$ and have been found to consist of a single absorption feature, even at 4 K, indicating the absence of charge disproportionation in this material.[35] The strong degree of similarity between the Fe XPS and XAS spectra for $SrFeO_3$ and those for the $n = 1$ SL supports the Fe^{4+} assignment in the latter.

Strong overlap between the Ni 2*p* and La 3*d* XPS core levels precludes determining the Ni valence for $n > 1$ because the latter dominates the former. Since the Ni 2*p* spectrum for the $n = 1$ SL strongly overlaps with that of $LaNi^{3+}O_3$ (Figure S4), we conclude that the Ni formal charge is 3+ in the $n = 1$ SL. In order to determine the Ni valence in SLs with $n > 1$, Ni *L*-edge XAS spectra in total fluorescence yield (TFY) mode were measured for select SLs. The long (~50 nm) attenuation length of the fluorescent x-rays in TFY mode led to significantly enhanced signal-to-noise ratios compared to those in TEY mode. As seen in Figure 2c, the Ni L_3 and L_2 edges for the $n = 1$ SL are very similar with that of $NdNiO_3$, which are split into two peaks (marked by magenta arrows, a sharp peak near 852 eV and a broad peak near 854 eV), corroborating the Ni^{3+} assignment in the $n = 1$ SL. This assignment is based on the fact that the same splitting occurs in experimental spectra for bulk rare-earth

nickelates (RNiO$_3$),[36] as well as in calculated spectra for Ni^{3+} in an octahedral crystal field.[37-39] The appearance of two peaks of Ni L edge spectra for Ni^{3+} might be ascribed to the dynamic charge disproportionation ($3d^8\underline{L} + 3d^8\underline{L} \rightarrow 3d^8 + 3d^8\underline{L}^2$, where $\underline{L}$ indicates a ligand hole).[40-44] In contrast, both Ni L_3 and L_2 edges of the n = 5 SL are singlets. As a result, the Ni L-edge spectrum of the n = 5 SL shows no evidence for charge disproportionation, but rather can be straightforwardly interpreted as indicating the presence of Ni^{4+} or, taking into account hybridization with O 2p states, $3d^8\underline{L}^2$. Indeed, the Ni L-edge spectrum for the n = 5 SL is very similar to the theoretically calculated spectrum of Ni^{4+} in an octahedral crystal field.[38,39] Moreover, the measured energy shift (~0.4 eV) of the Ni L_2 edge relative to that in NdNiO$_3$ also suggests that Ni in the n = 5 SL has a higher oxidation state than Ni^{3+}, i.e., it is closer to 4+.

The O K pre-edge feature is very sensitive to changes in the TM oxidation states and can be used to further corroborate our valence assignments.[45] To this end, we show the O K-edge XAS data for the n =1 and 5 SLs in Figure 2d. The broader pre-edge feature at ~527.5 eV for the n = 1 SL is also seen in cubic SrFeO$_3$, consistent with Fe^{4+} in the former.[46,47] The n = 5 SL exhibits two pre-peaks at 527.3 eV (A) and 529 eV (B) characteristic of oxygen 2p hybridization with Ni 3d and Fe 3d, respectively. The shape and position of feature B are similar to those seen in LaFeO$_3$, lending additional support to the Fe valence being 3+ in the n = 5 SL. Peak A is clearly located at a lower energy than the pre-edge feature measured for $LaNi^{3+}O_3$ (528 eV), corroborating the presence of Ni^{4+} in the n = 5 SL.

To better understand the dependence of the TM cation valences on SL periodicity, we investigate the band alignment for different SLs. Determining accurate valence band offsets from XPS as described by Kraut *et al.*[48] is precluded by the fact that a reference specimen of thick-film perovskite SNO could not be synthesized due to its instability. We thus utilize two approximate methods. **Figure 3a** illustrates the first of these. Here we use the VB spectra measured for thick epitaxial SrFeO$_3$ and LaNiO$_3$ films as proxies for Fe^{4+} and Ni^{3+},

respectively, in the n = 1 SL. We fit the n = 1 SL spectrum to a linear combination of these two spectra. The resulting valence band maxima (VBM, E_V) were determined by linear extrapolation of the leading edges of the component VB spectra to the energy axis. The valence band offset (VBO) is then given by $\Delta E_V = E_V(LaNi^{3+}O_3) - E_V(SrFe^{4+}O_3)$ = -0.20 eV, consistent with hole confinement in the LFO layers. A band-edge diagram for the n = 1 SL can be estimated and is shown in the upper part of Figure 3d. This method cannot be used for the n > 1 SLs, however, due to the absence of a suitable Ni^{4+}-containing reference perovskite for which a VB spectrum could be measured. We thus turn to a second method in which we isolate the contributions of SNO and LFO to the overall SL VB spectra. Figure 3b shows the VB spectra for a pure $LaFeO_3$ film along with those of three SNO_1/LFO_n (n = 3, 5, 8) SLs. All spectra were shifted in energy such that the corresponding La $3d_{5/2}$ peaks fall at the same binding energy as that for thick-film $LaFeO_3$. Based on the observation that the VBM values of SLs are lower in binding energy than that of pure LFO, we intuit that the top portions of the SL VBs are SNO derived. As a result, the VBO can be estimated as $\Delta E_V \approx E_V(LaFeO_3) - E_V(SL)$. The resulting ΔE_V values are plotted as blue solid circles in Figure 3c. With a ΔE_V value of ~0.55 eV, the SNO layers in the n = 5 SL contain potential wells of sufficient depth to strongly confine the holes to the SNO layers (Figure 3d), resulting in Ni^{4+} and Fe^{3+}.

In order to understand the nature of charge redistribution in these SLs as function of n, we turn to DFT simulations. The calculated geometrical structures for the n = 1, 3, and 5 SLs, all epitaxially strained to the LSAT substrate, are shown in **Figure 4a**. In all cases, the lowest energy configurations include *G*-type antiferromagnetic coupling within the LFO part of the system and *C*-type coupling in the adjacent NiO_2 and FeO_2 planes. Compared with the n = 1 SL, n = 3 and 5 SLs exhibit more obvious rotations of the FeO_6 and NiO_6 octahedra. The out-of-plane BO_6 octahedral tilt angle extracted from DFT calculations (**Figure S5**) ranges from 5 to 12° for the n = 5 SL, while it is only 2~3° for the n = 1 SL. In particular, our cross-sectional annular bright field (ABF) STEM images (Figure 4b and **Figure S6**) show that there is a clear

displacement of O positions commensurate with rotations of the FeO_6 and NiO_6 octahedra that is more pronounced in the n = 5 SL than the n = 1 SL. Moreover, our synchrotron X-ray superstructure half-order diffraction results show the presence of significantly more a^+/b^+ octahedral rotations and A-site displacements (**Figure S7**) in the n = 5 SL than the n = 1 SL. These results further confirm that oxygen octahedra rotations are strongly affected by the LFO layer thickness, suggesting that octahedral rotations are driven by the LFO portion of the SLs.

To examine how the magnitude of these rotations is coupled to the character of the charge density distribution, we compare the one-electron density of states (DOS) calculated for bulk LFO, also coherently strained to the LSAT substrate, for the cases of: (i) centro-symmetric positioning of all atoms, (ii) relaxation of atomic positions in the off-plane direction only (i.e., along the *c*-axis), and, (iii) fully-relaxed atomic positions. In all cases, the off-plane lattice parameter was optimized to minimize the total energy. These structures and the corresponding total DOS as well as the projections of the total DOS on the Fe atomic orbitals are shown in **Figure S8**. Notably, the primarily Fe 3*d* occupied band, located above the predominantly O 2*p*-derived band, shifts to a higher energy and spans a wider energy range if the LFO atoms are constrained to the centro-symmetric positions. This result suggests that if LFO is interfaced with another material that has an unoccupied band within ~2 eV of the top of the LFO O 2*p* band, the magnitude of the FeO_6 octahedral rotations can be used to control electron spillover from the Fe 3*d* band to the unoccupied states of the adjacent material.

To further quantify the coupling between the DOS and octahedral rotations, we performed similar calculations for the n = 1, n = 3, and n = 5 SLs. The energies of these systems were calculated with respect to their respective centro-symmetric configurations and are plotted in **Figure S9a**, along with the corresponding energies for LFO. In all cases, relaxation exclusively along the *c*-axis results in a significant energy gain that we attribute to the internal polarization that counteracts the polarity mismatch at the formally III-III LFO/II-

IV SNO interfaces. Octahedral rotations further stabilize these SLs, except for the n = 1 SL case where these rotations are not obvious. Furthermore, recalculating the energy gain due to overall relaxation on a per FeO_2 layer basis (Figure S9b) yields consistent values for LFO, n = 3 SL, and n = 5 SL systems but not for the n = 1 SL, indicating that the FeO_2 layers in the n = 1 SL do not retain their bulk LFO character. Given the dependence of LFO DOS on the geometrical structure (Figure S8), this result suggests that the $3d^5$ shell of Fe in the n = 1 SL is partially depleted, which is consistent with LFO-to-SNO electron transfer since Ni is the only other reducible species in the system.

This charge redistribution in the n = 1 SL would naturally lead to the formation of formally Fe^{4+} and Ni^{3+} ions in LFO and SNO, respectively, consistent with experiment (Figure 2). However, quantifying the associated charges from the DFT simulations is challenging. Indeed, previous analysis of the charge density redistribution induced by electron and hole trapping at transition metal species demonstrated that the density redistribution extends well beyond the nearest neighbors,[49] precluding a unique partitioning of this density over individual atoms. Rather, we chose to utilize the character of the DOS projected on the adjacent oxygen atomic orbitals as a qualitative measure of the charge transfer. **Figure S10** shows the total DOS and the O-projected DOS for the bulk LFO and $SrFe^{4+}O_3$. In the case of LFO (Fe^{3+}), there are no unoccupied O-derived bands just above the Fermi energy (E_F). In contrast, formally Ni^{3+} ions in LNO (Figure 4c) pull some electron density from the neighboring oxide ions, resulting in a small but detectable density of states at and above E_F. This effect is magnified in the case of SNO, where formally Ni^{4+} ions pull a significantly larger amount of electron charge from the neighboring O^{2-} ions, leading to an unoccupied band feature immediately above E_F. Such an unoccupied O-projected band close to E_F reveals the presence of holes.

Comparison of the O-projected DOS for the n = 5 SL (Figure 4d) with those for the reference materials described above suggests that the fully relaxed configuration restores the

Fe^{3+} valence state in LFO and induces unoccupied bands that resemble those in SNO near the NiO_2 plane. Thus, analysis of the character of the vacant bands in the O-projected DOS allows us to conclude that Fe and Ni in the fully relaxed n = 5 SL retain their primarily Fe^{3+} and Ni^{4+} valence character. We also examined the effects of A-site intermixing in the n = 5 SL using *ab initio* simulations and found that it has negligible effect on the thermodynamic stability, charge distribution and electronic structure (**Figures S11-S13**). In contrast, the presence (absence) of unoccupied O-projected DOS near E_F in the FeO_2 (NiO_2) planes point to Fe^{4+} and Ni^{3+} in the fully relaxed n = 1 SL (see Figure 4e). Such charge redistribution between LFO and SNO is also supported by the Bader population analysis of the oxygen species across the n = 1 SL and the n = 5 SL, as shown in **Figure S14**. Utilizing oxygen atomic charges as a signature the cation oxidation states, we find that in the n = 1 SL, the Fe valence is greater than 3+ in the LFO and is close to that of formally Fe^{4+}, as found in SFO. At the same time, the Ni valence is less than 4+ and is close to that in formal Ni^{3+}, as found in LNO. In contrast, the central part of the LFO in the fully relaxed n = 5 SL clearly preserves the LFO character, while the oxygens in the *A*O planes near the NiO_2 plane are less negative, indicating hole trapping that manifests itself in the formation of Ni^{4+}.

Based on the experimental observation of the valence change (Figure 2), the derived band-edge energy diagrams (Figure 3d), and the DFT calculations (Figure 4), we can begin to understand the in-plane transport behavior of these SLs. Resistivity versus temperature (ρ-T) curves for the SNO_1/LFO_n SLs are shown in Figure 3e along with data from a 20 nm fully oxidized $SrFeO_3$ film. The $SrFeO_3$ film shows metallic behavior down to the lowest temperature measured, while all SNO_1/LFO_n SLs exhibit semiconducting behavior. The ρ(300 K) value for the n = 1 SL is very close to that of the $SrFe^{4+}O_3$ film due to conduction in the LFO (Fe^{4+}) layers of the SL. ρ(T) increases for all T as the LFO layer thickness increases due to the growing dominance of insulating $LaFe^{3+}O_3$ layers. Comparison of the transport properties of solid solutions with the same volume-averaged compositions as the n = 1 and 5

SLs reveals markedly different behavior (**Figure S15**). This result illustrates the critical importance of nanoscale structuring in gaining control over emergent electronic properties.

In summary, we demonstrate that a rare high formal charge for Ni in perovskite oxides can be stabilized by artificially structuring its environment in superlattice form. We observe that perovskite SNO, which is not observed in bulk form, can be stabilized in the SNO_m/LFO_n superlattices, but only at the thickness of a single SNO unit cell (m = 1). By controlling the LFO layer thickness (n), we can selectively drive either Fe or Ni to the 4+ valence. DFT calculations reveal that charge transfer from Fe to Ni occurs in the n = 1 SL, inducing the charge reconstruction ($Fe^{3+} \rightarrow Fe^{4+}$ and $Ni^{4+} \rightarrow Ni^{3+}$) at the interface. Increasing n introduces larger octahedral rotations, causing the structural properties of the LFO layers to approach those of bulk LFO. This structural change modifies the electron densities of states, resulting in hole localization in the SNO layers and manifesting itself in the formation of Ni^{4+} in the n = 5 SL. Our results offer exciting opportunities to generate novel ground-states unobtainable in bulk crystals and suggest new strategies to achieve desired functional properties in correlated oxides by using the octahedral rotational proximity effect.

Supporting Information
Supporting Information is available from the Wiley Online Library or from the author.

Acknowledgements
This work is support by the U.S. Department of Energy (DOE), Office of Science, Office of Basic Energy Sciences, Division of Materials Sciences and Engineering under Award #10122. This research used resources of the Advanced Photon Source, a U.S. DOE Office of Science User Facility operated by Argonne National Laboratory under contract DE-AC02-06CH11357. The research was performed using EMSL, a DOE Office of Science User Facility sponsored by the Office of Biological and Environmental Research. Pacific Northwest National Laboratory (PNNL) is a multi-program national laboratory operated for DOE by Battelle. A portion of the microscopy work was performed in the Radiological Microscopy Suite (RMS), located in the Radiochemical Processing Laboratory (RPL) at PNNL. S. R. Spurgeon would like to thank Dr. Colin Ophus for assistance with the STEM data analysis. W. S. Samarakoon acknowledges the PNNL-OSU Fellowship.

Received: ((will be filled in by the editorial staff))
Revised: ((will be filled in by the editorial staff))
Published online: ((will be filled in by the editorial staff))

References

[1] H. Y. Hwang, Y. Iwasa, M. Kawasaki, B. Keimer, N. Nagaosa, Y. Tokura, *Nat. Mater.* **2012**, 11 (2), 103.

[2] R. Ramesh, D. G. Schlom, *Nat. Rev. Mater.* **2019**, 4, 257.

[3] A. Ohtomo, D. Muller, J. Grazul, H. Y. Hwang, *Nature* **2002**, 419 (6905), 378.

[4] S. Thiel, G. Hammerl, A. Schmehl, C. Schneider, J. Mannhart, *Science* **2006**, 313 (5795), 1942-1945.

[5] S. J. May, P. Ryan, J. Robertson, J.-W. Kim, T. S. Santos, E. Karapetrova, J. L. Zarestky, X. Zhai, S. Te Velthuis, J. N. Eckstein, S. D. Bader, A. Bhattacharya, *Nat. Mater.* **2009**, 8 (11), 892.

[6] J. Kleibeuker, Z. Zhong, H. Nishikawa, J. Gabel, A. Müller, F. Pfaff, M. Sing, K. Held, R. Claessen, G. Koster, G. Rijnders, *Phys. Rev. Lett.* **2014**, 113 (23), 237402.

[7] Y. Cao, X. Liu, M. Kareev, D. Choudhury, S. Middey, D. Meyers, J.-W. Kim, P. Ryan, J. Freeland, J. Chakhalian, *Nat. Commun.* **2016**, 7, 10418.

[8] M. Grisolia, J. Varignon, G. Sanchez-Santolino, A. Arora, S. Valencia, M. Varela, R. Abrudan, E. Weschke, E. Schierle, J. E. Rault, J.-P. Rueff, A. Barthélémy, J. Santamaria, M. Bibes, *Nat. Phys.* **2016**, 12 (5), 484.

[9] H. Lee, N. Campbell, J. Lee, T. Asel, T. Paudel, H. Zhou, J. Lee, B. Noesges, J. Seo, B. Park, L. J. Brillson, S. H. Oh, E. Y. Tsymbal, M. S. Rzchowski, C. B. Eom, *Nat. Mater.* **2018**, 17 (3), 231.

[10] H. Chen, A. Millis, *J. Phys. Condens. Matter* **2017**, 29 (24), 243001.

[11] S. Catalano, M. Gibert, J. Fowlie, J. Iniguez, J.-M. Triscone, J. Kreisel, *Rep. Prog. Phys.* **2018**, 81 (4), 046501.

[12] S. May, C. Smith, J.-W. Kim, E. Karapetrova, A. Bhattacharya, P. Ryan, Phys. Rev. B 2011, 83 (15), 153411.

[13] J. M. Rondinelli, S. J. May, J. W. Freeland, *MRS bulletin* **2012**, 37 (3), 261-270.

[14] J. Chaloupka, G. Khaliullin, *Phys. Rev. Lett.* **2008**, 100 (1), 016404.

[15] P. Hansmann, X. Yang, A. Toschi, G. Khaliullin, O. Andersen, K. Held, *Phys. Rev. Lett.* **2009**, 103 (1), 016401.

[16] S. Dong, E. Dagotto, *Phys. Rev. B* **2013**, 87 (19), 195116.

[17] M. Gibert, M. Viret, A. Torres-Pardo, C. Piamonteze, P. Zubko, N. Jaouen, J.-M. Tonnerre, A. Mougin, J. Fowlie, S. Catalano, A. Gloter, O. Stéphan, J.-M. Triscone, *Nano Lett.* **2015**, 15 (11), 7355-7361.

[18] M. Gibert, P. Zubko, R. Scherwitzl, J. Íñiguez, J.-M. Triscone, *Nat. Mater.* **2012**, 11 (3), 195.

[19] X. Liu, M. Kotiuga, H.-S. Kim, Y. Choi, Q. Zhang, Y. Cao, M. Kareev, F. Wen, B. Pal, J. W. Freeland, L. Gu, D. Haskel, P. Shafer, E. Arenholz, K. Haule, D. Vanderbilt, K. M. Rabe, J. Chakhalian, *Proc. Natl. Acad. Sci. U.S.A* **2019**, 116, 19863.

[20] A. Boris, Y. Matiks, E. Benckiser, A. Frano, P. Popovich, V. Hinkov, P. Wochner, M. Castro-Colin, E. Detemple, V. K. Malik, C. Bernhard, T. Prokscha, A. Suter, Z. Salman, E. Morenzoni, G. Cristiani, H.-U. Habermeier, B. Keimer, *Science* **2011**, 332 (6032), 937-940.

[21] E. Benckiser, M. W. Haverkort, S. Brück, E. Goering, S. Macke, A. Frañó, X. Yang, O. K. Andersen, G. Cristiani, H.-U. Habermeier, A. V. Boris, I. Zegkinoglou, P. Wochner, H.-J. Kim, V. Hinkov, B. Keimer *Nat. Mater.* **2011**, 10 (3), 189.

[22] A. J. Grutter, H. Yang, B. J. Kirby, M. Fitzsimmons, J. A. Aguiar, N. D. Browning, C. Jenkins, E. Arenholz, V. Mehta, U. Alaan, Y. Suzuki, *Phys. Rev. Lett.* **2013**, 111 (8), 087202.

[23] S. Middey, J. Chakhalian, P. Mahadevan, J. Freeland, A. J. Millis, D. Sarma, *Annual Review of Materials Research* **2016**, 46, 305-334.

[24] M. D. Scafetta, A. M. Cordi, J. M. Rondinelli, S. J. May, *J. Phys. Condens. Matter* **2014**, 26 (50), 505502.

[25] P. C. Rogge, R. U. Chandrasena, A. Cammarata, R. J. Green, P. Shafer, B. M. Lefler, A. Huon, A. Arab, E. Arenholz, H. N. Lee, T.-L. Lee, S. Nemšák, J. M. Rondinelli, A. X. Gray, S. J. May, *Phys. Rev. Mater.* **2018**, 2 (1), 015002.

[26] J. Liu, E. Jia, L. Wang, K. A. Stoerzinger, H. Zhou, C. S. Tang, X. Yin, X. He, E. Bousquet, M. E. Bowden, A. T. S. Wee, S. A. Chambers, Y. Du, *Adv. Sci.* **2019**, 6, 1901073.

[27] Z. Liao, M. Huijben, Z. Zhong, N. Gauquelin, S. Macke, R. Green, S. Van Aert, J. Verbeeck, G. Van Tendeloo, K. Held, G. A. Sawatzky, G. Koster, G. Rijnders, *Nat. Mater.* **2016**, 15 (4), 425.

[28] A. Mercy, J. Bieder, J. Íñiguez, P. Ghosez, *Nat. Commun.* **2017**, 8 (1), 1677.

[29] A. Blanca-Romero, R. Pentcheva, *Phys. Rev. B* **2011**, 84 (19), 195450.

[30] Y. Takeda, T. Hashino, H. Miyamoto, F. Kanamaru, S. Kume, M. Koizumi, *Journal of Inorganic and Nuclear Chemistry* **1972**, 34 (5), 1599-1601.

[31] H. Seki, T. Saito, Y. Shimakawa, *J. Jpn. Soc. Powder Powder Metall.* **2016**, 63 (7), 609-612.

[32] S. Chakraverty, T. Matsuda, N. Ogawa, H. Wadati, E. Ikenaga, M. Kawasaki, Y. Tokura, H. Hwang, *Appl. Phys. Lett.* **2013**, 103 (14), 142416.

[33] T. Tsuyama, T. Matsuda, S. Chakraverty, J. Okamoto, E. Ikenaga, A. Tanaka, T. Mizokawa, H. Hwang, Y. Tokura, H. Wadati, *Phys. Rev. B* **2015**, 91 (11), 115101.

[34] L. Wang, Y. Du, P. V. Sushko, M. E. Bowden, K. A. Stoerzinger, S. M. Heald, M. D. Scafetta, T. C. Kaspar, S. A. Chambers, *Phys. Rev. Mater.* **2019**, 3 (2), 025401.

[35] M. Takano, J. Kawachi, N. Nakanishi, Y. Takeda, *J. Solid State Chem.* **1981**, 39 (1), 75-84.

[36] J. W. Freeland, M. Van Veenendaal, J. Chakhalian, *J. Electron Spectros. Relat. Phenomena* **2016**, 208, 56-62.

[37] C. Lenser, Q. Lu, E. Crumlin, H. Bluhm, B. Yildiz, *J. Phys. Chem. C* **2018**, 122 (9), 4841-4848.

[38] Q. Li, R. Qiao, L. A. Wray, J. Chen, Z. Zhuo, Y. Chen, S. Yan, F. Pan, Z. Hussain, W. Yang, *J. Phys. D Appl. Phys.* 2016, 49 (41), 413003.

[39] R. Qiao, L. A. Wray, J.-H. Kim, N. P. Pieczonka, S. J. Harris, W. Yang, *J. Phys. Chem. C* **2015**, 119 (49), 27228-27233.

[40] T. Mizokawa, D. Khomskii, G. Sawatzky, *Phys. Rev. B* **2000**, *61* (17), 11263.

[41] H. Park, A. J. Millis, C. A. Marianetti, *Phys. Rev. Lett.* **2012**, 109 (15), 156402.

[42] S. Johnston, A. Mukherjee, I. Elfimov, M. Berciu, G. A. Sawatzky, *Phys. Rev. Lett.* **2014**, 112 (10), 106404.

[43] J. Varignon, M. N. Grisolia, J. Íñiguez, A. Barthélémy, M. Bibes, *npj Quantum Mater.* **2017**, 2 (1), 1-9.

[44] R. J. Green, M. W. Haverkort, G. A. Sawatzky, *Phys. Rev. B* **2016**, 94 (19), 195127.

[45] R. Qiao, S. Roychoudhury, Z. Zhuo, Q. Li, Y. Lyu, J.-H. Kim, J. Liu, E. Lee, B. J. Polzin, J. Guo, S. Yan, Y. Hu, H. Li, D. Prendergast, W. Yang, doi.org/10.26434/chemrxiv.11416374.v2 (2019).

[46] C. Ge, C. Liu, Q. Zhou, Q. Zhang, J. Du, J. Li, C. Wang, L. Gu, G. Yang, K. Jin, *Adv. Mater.* **2019**, 31, 1900379.

[47] V. R. Nallagatla, T. Heisig, C. Baeumer, V. Feyer, M. Jugovac, G. Zamborlini, C. M. Schneider, R. Waser, M. Kim, C. U. Jung, R. Dittmann, *Adv. Mater.* **2019**, 31, 1903391.

[48] E. Kraut, R. Grant, J. Waldrop, S. Kowalczyk, *Phys. Rev. Lett.* **1980**, 44 (24), 1620.

[49] H. Raebiger, S. Lany, A. Zunger, *Nature* **2008**, 453 (7196), 763-766.

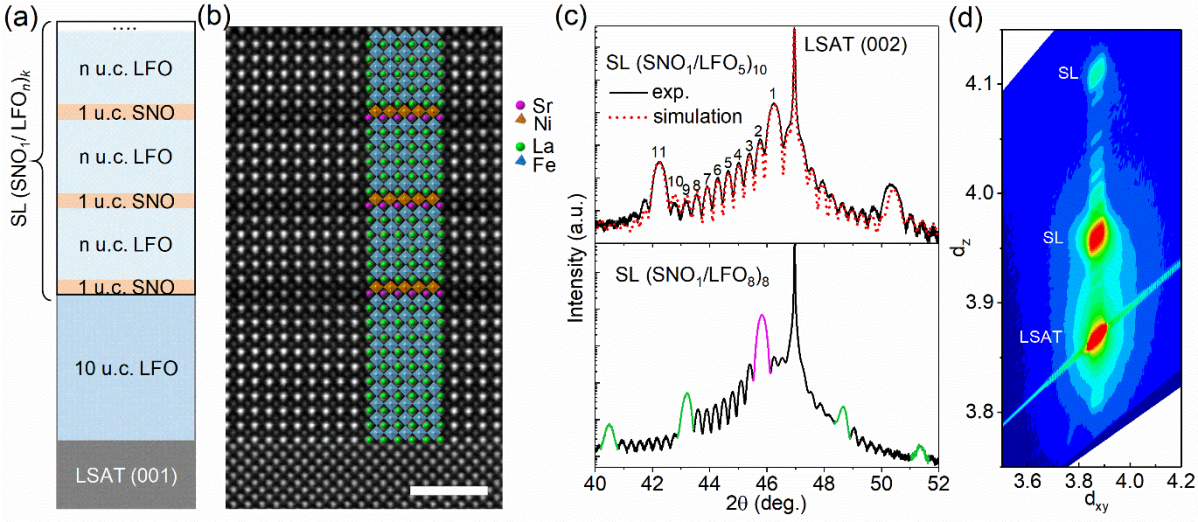

Figure 1. Synthesis of epitaxial $(SNO_1/LFO_n)_k$ SLs and structural characterization. (a) Structural diagram for the 10 u.c. LFO-buffered $(SNO_1/LFO_n)_k$ SL. (b) Cross-sectional HAADF STEM image of the n = 5 SL along the [100] substrate orientation. Structure assignments are also shown for comparison. The scale bar is 2 nm. (c) Experimental X-ray diffraction θ-2θ scans for the n = 5 and 8 SLs. The red dots denote the simulation results. By way of example, the purple feature corresponds to the main SL peak and yields the average c-axis parameter and the green peaks indicate the higher-order SL satellite peaks. (d) Reciprocal space map near the 103 reflection for the n = 8 SL, confirming structural coherence.

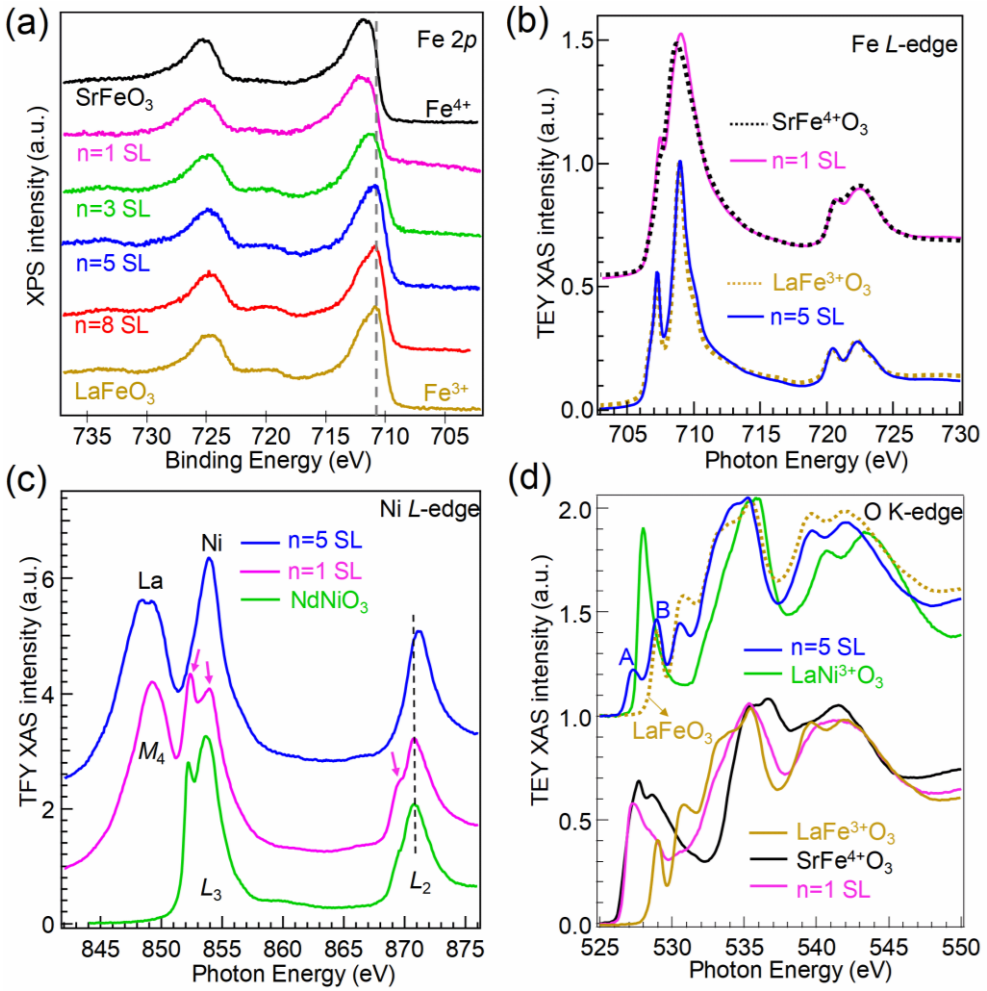

Figure 2. Selective control of Ni^{4+} and Fe^{4+} by tuning *n* in SNO_1/LFO_n SLs. The reference spectra for Fe^{4+} and Fe^{3+} were measured using an oxygen plasma annealed $SrFe^{4+}O_3$ and $LaFe^{3+}O_3$ films, respectively. (a) *In situ* Fe 2*p* XPS. The dashed grey line denotes the Fe 2*p* binding energy for $LaFe^{3+}O_3$. (b) Fe *L*-edge XAS. (c) Ni *L*-edge XAS. (d) O *K*-edge XAS. Features in the low-energy portion of the *n* = 5 SL spectra are denoted as A and B. All Fe *L*-edge and O *K*-edge spectra were collected in the more surface-sensitive total electron yield (TEY) detection mode, while all Ni *L*-edge spectra of SLs were collected using the more bulk-sensitive total fluorescence yield (TFY) detection mode at room temperature. Ni *L*-edge XAS measured with an insulating $NdNiO_3$ film at 100 K was used as a reference in (c). O *K*-edge XAS measured with a $LaNiO_3$ film was used as a reference in (d).

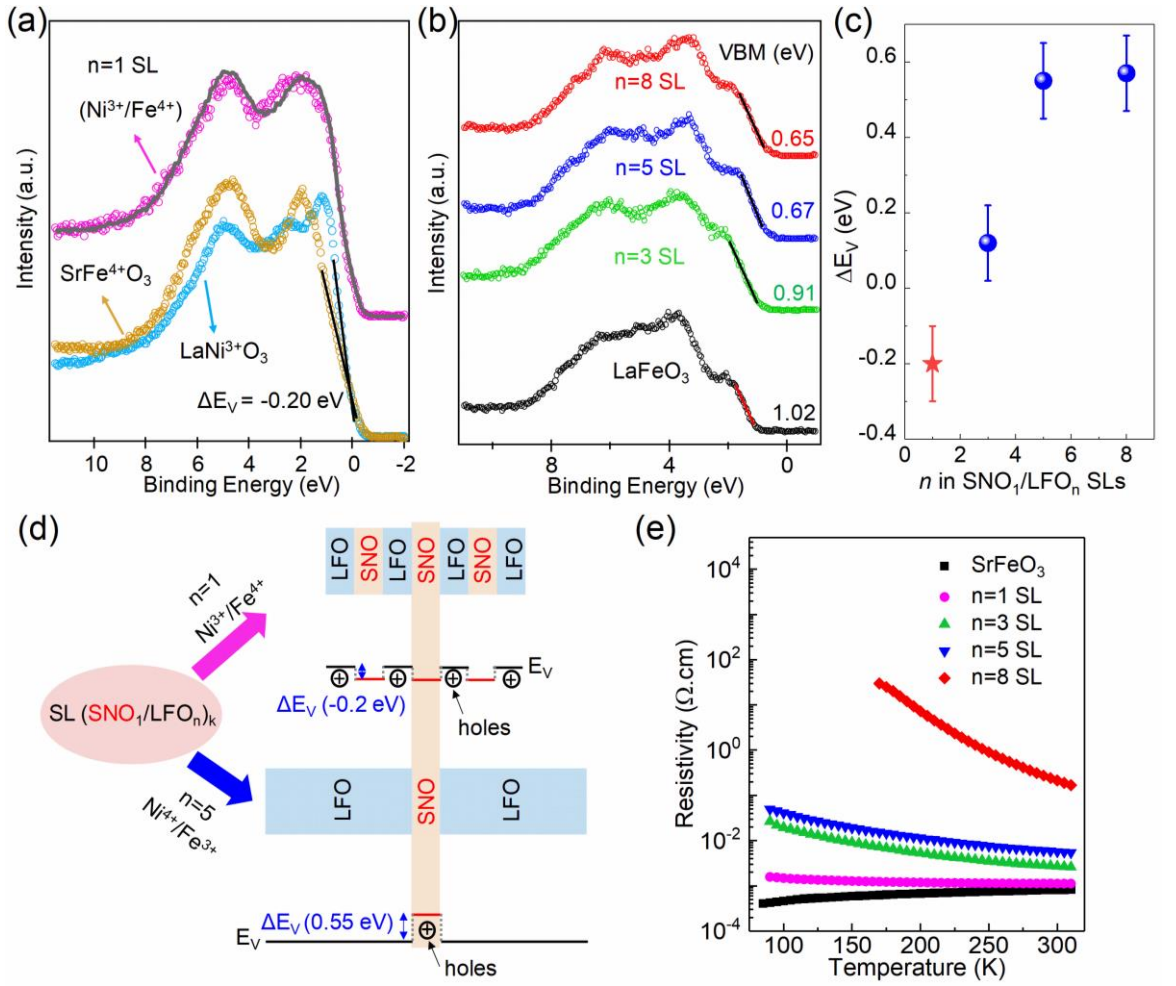

Figure 3. Valence band offset (VBO) analysis and in-plane transport properties. (a) Approach 1: Estimating the VBO for the *n* = 1 SL by simulating the SL valence band (VB) spectrum using a linear combination of VB spectra for phase pure perovskites containing Ni^{3+} and Fe^{4+}. The *n* = 1 SL VB spectrum is well reproduced by such a linear combination (grey) of spectra for pure $LaNiO_3$ (blue) and pure $SrFeO_3$ (yellow), appropriately weighted and shifted to reflect the physical structure (purple). (b) VB spectra for pure $LaFeO_3$ and SNO_1/LFO_n SLs with *n* ranging from 3 to 8. Approach 2: The VBOs are estimated by taking the differences between the leading edges extrapolated to the energy axis for the various SLs and that for pure LFO (see text for rationale). (c) ΔE_V values deduced from (a) and (b) are shown as a red star and blue solid circles, respectively. (d) Energy band-edge diagrams for the *n* = 1 and *n* = 5 SLs resulting from band alignment analysis. (e) Resistivity versus temperature (ρ-T) curves for SNO_1/LFO_n SLs (*n* = 1, 3, 5, 8) and a 20 nm $SrFeO_3$ film.

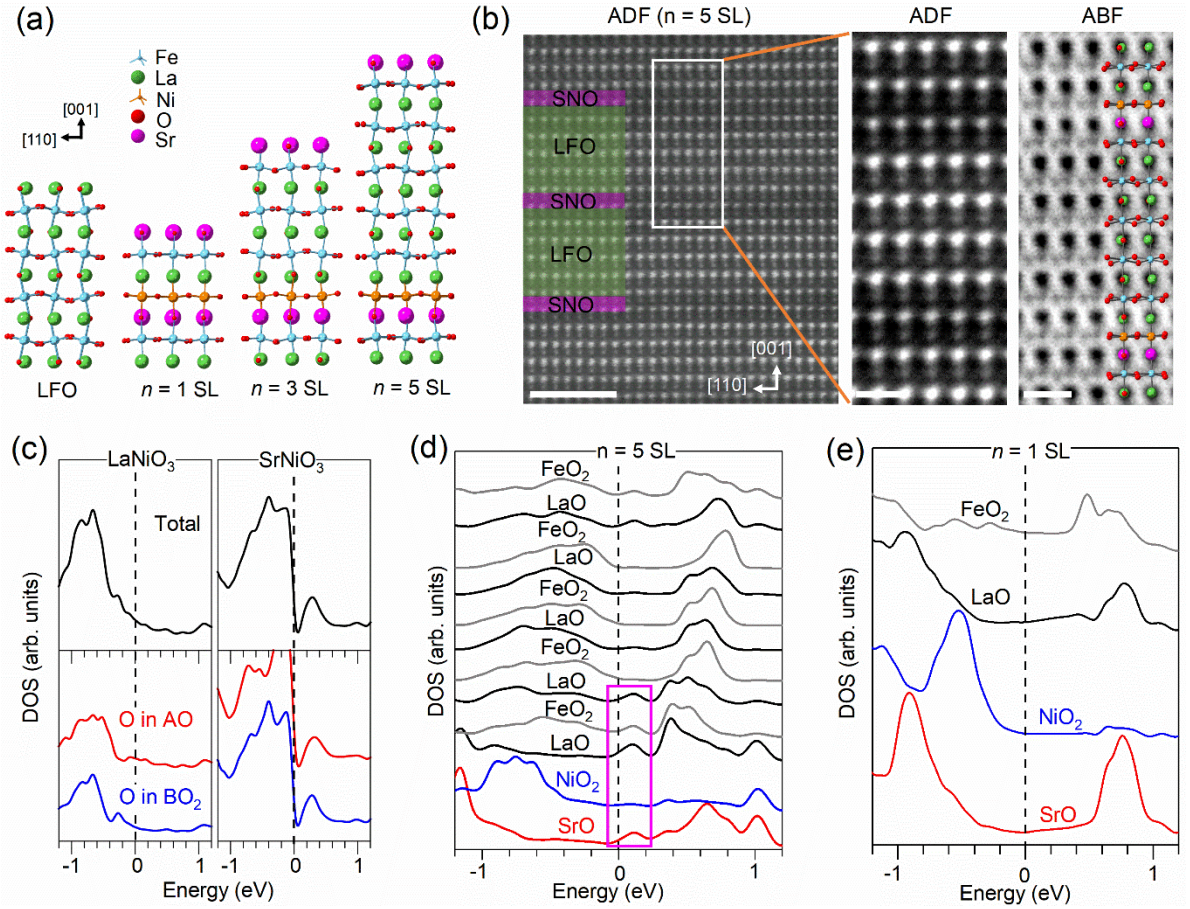

Figure 4. DFT calculations results and octahedral rotations observed in ABF STEM images. (a) The optimized geometrical structures of LFO and the SNO_1/LFO_n SLs. Distinct oxygen octahedral rotations with increasing *n* are observed. (b) Cross-sectional ADF STEM image (left) of the *n* = 5 SL along the [110] substrate orientation. The scale bar is 2 nm. Magnified template-matched ADF STEM image and corresponding ABF STEM image with a scale bar of 0.5 nm are shown at the right. The DFT simulated structure of the *n* = 5 SL viewed along [1-10] direction is also overlaid for comparison. (c) One-electron density of states (DOS) near E_F for the bulk $LaNiO_3$ and $SrNiO_3$ epitaxially strained to the LSAT substrate: total DOS (top panel) and the DOS projected on the atomic orbitals of oxygen atoms (bottom panel). All plots are aligned to place E_F at 0 eV. (d, e) Density of states near E_F projected on the oxygen atomic orbitals for the *n* = 5 SL (d) and *n* = 1 SL (e) in the fully relaxed configuration. Red, blue, black and gray lines correspond to the SrO, NiO_2, LaO and FeO_2 parts of the SL, respectively. Purple rectangle in (d) highlights the DOS features corresponding to holes localized on the oxygen states.

The otherwise unstable Ni^{4+} can be stabilized in perovskite oxides by artificial structuring in carefully designed $(SrNiO_3)_1/(LaFeO_3)_n$ superlattices. Spectroscopy measurements in combination with DFT calculations reveal that B-site cation valences can be tuned by controlling the magnitude of the FeO_6 octahedral rotations which in turn drive the energy balance between Ni^{3+}/Fe^{4+} and Ni^{4+}/Fe^{3+}, thus controlling emergent electrical properties.

Perovskite oxide superlattices

Le Wang, Zhenzhong Yang, Mark E. Bowden, John W. Freeland, Peter V. Sushko, Steven R. Spurgeon, Bethany Matthews, Widitha S. Samarakoon, Hua Zhou, Zhenxing Feng, Mark H. Engelhard, Yingge Du*, and Scott A. Chambers*

Hole-Trapping-Induced Stabilization of Ni^{4+} in $SrNiO_3/LaFeO_3$ Superlattices